Visualizing In-Plane Junctions in Nitrogen-Doped Graphene

Mehdi Bouatou, Cyril Chacon, Aleksander Bach Lorentzen, Huu Thoai Ngo, Yann Girard, Vincent Repain, Amandine Bellec, Sylvie Rousset, Mads Brandbyge, Yannick Dappe, et al.

Visualizing in-plane junctions in nitrogen-doped graphene

Mehdi Bouatou Cyril Chacon Aleksander Bach Lorentzen Huu Thoai Ngo Yann Girard Vincent Repain Amandine Bellec Sylvie Rousset Mads Brandbyge Yannick J. Dappe Jérôme Lagoute

Dr. M. Bouatou, Dr. C. Chacon, Mr. Huu Thoai Ngo, Dr. Y. Girard, Prof V. Repain, Dr. A. Bellec, Dr. A. Rousset, Dr. J. Lagoute
Laboratoire Matériaux et Phénomènes Quantiques, CNRS-Université Paris Cité, 10 rue Alice Domon et Léonie Duquet, 75205 Paris Cedex 13, France.
jerome.lagoute@u-paris.fr
Mr. A. Bach Lorentzen, Prof. M. Brandbyge
Center for Nanostructured Graphene, Department of Physics,Technical University of Denmark, DK-2800 Kongens Lyngby, Denmark.
Dr. Y. J. Dappe
SPEC, CEA, CNRS, Université Paris-Saclay, CEA Saclay, 91191 Gif-sur-Yvette Cedex, France

Controlling the spatial distribution of dopants in graphene is the gateway to the realization of graphene-based electronic components. Here, we show that a submonolayer of self-assembled physisorbed molecules can be used as a resist during a post-synthesis nitrogen doping process to realize a nanopatterning of nitrogen dopants in graphene. The resulting formation of domains with different nitrogen concentrations allows obtaining nn' and pn junctions in graphene. We use scanning tunneling microscopy to measure the electronic properties of the junctions at the atomic scale and reveal their intrinsic width that is found to be around 7 nm corresponding to a sharp junction regime.

1 Introduction

Mastering the doping of materials is the foundation of microelectronics. The control of the bandstructure of crystals by traces of dopants allows the realization of pn junctions which are fundamental building blocks for electronic devices. In the search for post-silicon technology, new promises have arisen with the discovery of graphene and two-dimensional materials.

Soon after the first isolation of graphene, its chemical doping has been investigated [1] with particular attention in nitrogen doping which is an n-type dopant [2, 3, 4]. To bring graphene to a new level, the next challenge is to control the spatial distribution of dopants. This would allow band engineering in graphene to be performed in a manner similar to what is done in semiconductor devices. Different ways have been used to realize pn junctions in graphene. Conventional in-plane junctions are usually realized with gate electrodes using electrostatic doping. The width of the potential step in these setups depends on the device geometry and can be reduced down to 40 nm in the best case [5]. Substrate engineering has been used to induce potential wells in graphene through variations of substrate surface reconstruction [6], vacancy islands [7], interfacial charge transfer in graphene/α-RuCl$_3$ heterostructures [8]. Controlled local doping has been achieved by combining STM tip manipulation with back gate electrode [9, 10]. In these works, the doping was achieved by the interaction of pure graphene with the environment. The interaction of graphene with molecules such as C$_{60}$ has also been widely studied [11, 12, 13, 14, 15]. In the case of chemical doping, selective doping during growth has been realized to obtain pn junctions by growing graphene on a chemically prepatterned substrate [16]. In that work the p-doped and n-doped domains have been investigated separately at the atomic scale by scanning tunneling microscopy (STM), but the junction between the domains could not be addressed due to the difficulty to address a single junction in a large sample with a local probe.

Some key questions are still pending regarding the properties of in-plane junctions in chemically doped graphene. The structure of such junctions at the atomic scale and the width of the space charge region remain unknown. To answer these questions, an investigation of the structure and electronic properties at the atomic scale is needed, and can be achieved using STM in an ultra high vacuum (UHV) environment. In order to have an easy access to the junctions by STM, a distribution of junctions on the whole

surface of a sample is desirable. Here, we address these questions, and in order to obtain a collection of junctions in a sample, we provide a new route to control the spatial distribution of nitrogen dopants in graphene using self-assembled monolayer islands of C_{60} molecules as a molecular resist during post synthesis nitrogen doping. One advantage of this strategy is that it is a post-synthesis method, which allows to treat any graphene sample independently of the growth method. This method leads to the formation of a large collection of domains on a sample, allowing us to address the junctions at the atomic scale by STM. Compared to conventional lithography resist, the use of a physisorbed molecular monolayer deposited under UHV conditions makes it possible to avoid the presence of polymer residues and to achieve a significantly higher degree of cleanliness of the sample, which is mandatory for this study. One can note however that specific cleaning procedures can also be used to improve the cleanness of the surface when photoresist chemical compounds are used [17]. It has to be noted that the junctions investigated here have a different nature from the electrostatic or substrate engineering junctions. In the present case, the junctions are obtained by a spatial variation of the concentration of dopants, an analogue of standard pn junctions in semiconductors, whereas in other cases the junctions are induced by the environment of a pristine graphene layer. One interest of chemically doped graphene is its stability and the possibility to be transferred on different substrates or devices. Moreover previous work have shown that nitrogen dopants do not alter the bandstructure of graphene [18].

2 Results and discussion

We start with the demonstration that single layer C_{60} islands can be used as a resist to pattern the concentration of nitrogen dopants in graphene. All STM measurements were performed under ultrahigh vacuum (UHV) conditions at low temperature (4.6 K) on multilayer graphene grown on the carbon rich SiC(000$\bar{1}$) (See supplementary materials). The deposition of a submonolayer of C_{60} on graphene yields to compact C_{60} monolayer islands possibly including a native second layer that appears as bright protrusions on top of the monolayer islands (Figs. 1A, S1, S2). The basic idea of the submonolayer molecular resist is sketched in Fig. 1B. The C_{60}/graphene sample is exposed to activated nitrogen atoms produced by a plasma source [19]. The sp^2 carbon atoms of C_{60} are expected to react with nitrogen similarly to the sp^2 carbon atoms of graphene, thus preventing the reaction of nitrogen with graphene. We have tested this idea by exposing a C_{60}/graphene sample to a nitrogen plasma source. An image of the sample after plasma exposure is shown in Fig. 1C. Bright spots in the molecular island indicate that the C_{60} molecules have been effectively reacting with nitrogen. Substitutional nitrogen atoms appear on the surrounding graphene as bright dots [20, 19, 18].

In order to check the effect of C_{60}, we remove the C_{60} island by nanoshaving (sweeping the molecules with the STM tip [21]). This procedure consist in scanning the surface with a reduced tip-sample distance (large current, low bias voltage) at high speed. Although the parameters may be adjusted during the procedure, we have used typically a sample bias voltage of 0.1 V and a current setpoint of 1 nA with a scanning speed of 1.7 μm/s. During the procedure, intermediate images were acquired to check the state of the sample. The surface after 3 hours of molecule removal procedure is shown in Fig. 1D. The nitrogen concentration is lower below the molecular island (0.06%) than around it (0.17%), with a ratio corresponding to 65% of incoming nitrogen atoms stopped by the molecular layer. This partial efficiency can be understood considering that there is free space between the molecules in the C_{60} lattice (see supporting information). This observation suggest to test other molecules in future works in order to improve this ratio. Other measurements give average efficiencies of 62% (Fig. S3). One advantage of physisorbed molecular resist is its soft and non invasive nature, the molecules can easily be removed without inducing any defect in graphene. A more general procedure can be used by removing the molecules by thermal annealing. Therefore, nanodomain patterning of nitrogen in graphene can be achieved in a three steps process (Fig. 1E). A large scale STM image after annealing at 600°C is shown in Fig. 1F. Clearly, domains with low nitrogen concentration can be seen, which are a fingerprint of the C_{60} islands before annealing. This shows unambiguously that physisorbed C_{60} islands constitute an effective mask to induce nanostructuration of nitrogen dopants in graphene.

We turn now to the electronic properties of the junctions made of adjacent domains with different nitrogen concentrations. The graphene area shown in Fig. 2A contains a larger concentration of nitrogen in the right part than in the left part. dI/dV spectra measured on each region are characteristic of n-doped graphene. The gap-like feature around the Fermi level corresponds to the well-known inelastic excitation of a phonon mode of graphene [22]. The Dirac point is marked by a dip in the dI/dV curve at the voltage V_D [22, 20, 19, 18] below the Fermi level indicating the expected n-type doping. The spectra clearly show a larger downshift of the Dirac point on the high nitrogen concentration part (-0.21 V) (Fig. 2B) than on the low nitrogen concentration part (-0.09 V). More understanding is provided by the spatial variation of the Dirac point obtained by a dI/dV mapping at an energy slightly below the Dirac point [23, 24], or by measuring a dI/dV spectrum and extracting V_D at each pixel of an image [23, 25, 26, 18, 24]. In Fig. 2C, we show a conductance map measured at -0.3 V exhibiting a higher conductance on the low doped region and a lower conductance on the high doped region. This contrast is expected [22] since, at this bias voltage, the dI/dV signal lies around the minimum at V_D for the highly-doped part, while it lies in the increasing part of the dI/dV curve for the weakly-doped part. This area constitutes a unipolar nn' junction. The clear contrast and sharp boundary between the two parts constituting the junction allows us to estimate the area of each domain and to estimate the nitrogen concentration that is found to be 0.22 % on the high doped part and 0.06 % on the low doped part. A closer view of another junction is shown in Fig. 2D. The left part has a larger doping than the right part, the atomic resolution allows to identify each doping site in that image (Fig. S4). Using the conductance and the topographic image, we evaluated the nitrogen concentration following the same procedure as described above and we obtained 0.28 % on the high doped region and 0.08 % on the low doped region. The difference in the doping level of the two parts is reflected in the spectra of Fig. 2E. A quantitative mapping of the Dirac point position has been obtained by measuring a dI/dV spectrum and determining the Dirac point at each pixel of the image. The result is shown in Fig. 2F. A linescan over the junction shows the variation of the Dirac point (Fig. 2G). The width d of the junction is calculated using a fitting profile with the function[27], $V(x) = V_0 + V_1 \tanh\left(\frac{x-x_0}{\Delta}\right)$. We take the value 4Δ as an estimate of the barrier width (cutting the step profile at 96% of the values on both sides of the junction). We determine a width of the junction of 7.7 nm. A more systematic measurement on several linescans taken over three different mappings gives an average value of 7.1 nm with a standard deviation of 2.9 nm (Fig. S5). We also measured a conductance map on the same area (Fig. 2H) together with a linescan. The width of the junction has been determined using the same fitting procedure, and a statistics of linescans measured on three different conductance maps gives an average value of 7.2 nm with a standard deviation of 1.6 nm (Fig. S5). This finding opens new opportunities for probing the transport properties in sharp junctions. Dual probe STM experiments could be envisaged for measuring the transport though such junctions for example. In transport devices, C_{60} mask may possibly be patterned using atomic force microscopy followed by nitrogen plasma exposition in order to realize transport experiments through nitrogen doped graphene junctions.

In order to simulate the evolution of the Dirac point energy and to compare it to the experimental evolution shown in Figure 2F and 2G, we have designed a model n-n' graphene junction unit cell. Namely, we have considered a 116.4 Å × 74.4 Å rectangular unit cell of graphene of about 3500 atoms, with 3 substituting nitrogen atoms on one side of the cell, and 1 substituting nitrogen atom on the other side, following the experimental conditions. The two groups of atoms are separated by a distance of 69.4 Å. This unit cell is represented in the top of Figure 2I. Then we have calculated the projected density of states (PDOS) for successive slices of graphene along the length of the unit cell (see Methods for details). These calculations have been performed using Density Functional Theory (DFT). For each calculated PDOS, we have extracted the position of the local Dirac point, similarly to what has been measured in the linescan of Figure 2F. The corresponding evolution of the Dirac point energy is represented in the red curve of Figure 2I. The two pairs of blue vertical lines delimit the regions containing the group of 3 nitrogen atoms (on the left) and the single nitrogen atom (on the right). One can clearly observe a variation of the Dirac point energy, from an n doped region on the left at about -0.22 eV, to an almost neutral region on the right at about -0.07 eV. These findings are in good agreement with the experimen-

tal evolution shown in Figure 2G. Some extra variations of the Dirac point energy are also observed in the vicinity of the nitrogen atoms, with a minimum at -0.36 eV (left side) and another one at -0.22 eV (right side). This can be related to the local redistribution of electronic density induced by the nitrogen atoms, as represented in the charge isosurface of Figure 2I. It is worth to notice that close to a junction the charge redistribution of the nitrogen atoms is influenced by the potential gradient similarly to a standard semiconducting pn junction (see supporting informations Fig. S6).

In addition to the variation of the Dirac point, we have investigated the variation of interlayer interaction and local work function in a junction. On multilayer graphene, the rotational disorder between adjacent top layers eventually leads to the formation of moiré patterns and van Hove singularities (vHs) [28]. In Fig. 3A we show a graphene area with a moiré pattern of periodicity $\lambda = 1.64$ nm. dI/dV spectra measured on the two parts with different doping levels show a shift of E_D and vHs in the same direction (see Fig. 3B). It is worth to notice that the position of the vHs peaks are not symmetric with respect to V_D. On the highly doped part, $V_D = -0.2$ V and the peak positions of the vHs are $V_{\mathrm{vHs}^+} = 0.82$ V and $V_{\mathrm{vHs}^-} = -0.83$ V. This gives highly asymmetric positions with respect to V_D with $V_{\mathrm{vHs}^+} - V_D = 1.02$ V and $V_{\mathrm{vHs}^-} - V_D = -0.63 V$. After renormalization by the phonon inelastic excitation energy [22] the actual energies of the vHs with respect to the Dirac point can be obtained $E_{\mathrm{vHs}^+} = 0.90$ eV and $E_{\mathrm{vHs}^-} = -0.63$ eV (see supporting informations). This result is different from the standard case where the energy position of the vHs at positive and negative energy $E_{\mathrm{vHs}^\pm}^0$ are symmetric with respect to the Dirac point E_D following the relation $E_{\mathrm{vHs}^\pm}^0 - E_D = \pm\hbar\Gamma K sin(\Theta/2)v_F \mp t$. In this relation, $\hbar$ is the reduced Planck's constant, ΓK is the length of the reciprocal vector at the K point, Θ is the angle between the two graphene layers, v_F is the Fermi velocity of graphene and t is the interlayer coupling energy. Here the asymmetry is due to the fact that the top graphene layer is doped and interacts with the undoped underlying layer (see the inset in Fig. 3B). Considering the Dirac energy of the top layer E_{D_1} and the Dirac energy of the layer below E_{D_2}, the vHs energies become (more details in supporting informations and Fig. S7): $E_{\mathrm{vHs}^\pm} - E_{D_1} = E_{\mathrm{vHs}^\pm}^0 + (E_{D_2} - E_{D_1})/2$.

Taking $v_F = 10^6$ m/s, $t = 0.1$ eV, $sin(\Theta/2) = 0.123/\lambda$ and $E_{D_2} - E_{D_1} = 0.2$ eV, we obtain $E_{\mathrm{vHs}^+} = 0.84$ eV and $E_{\mathrm{vHs}^-} = -0.64$ eV in good agreement with the experimental values. Interestingly, these relations can be reversed to deduce the Dirac point energy when its direct determination is rendered difficult by the proximity with the phonon feature. On the lower doped part the peaks of the vHs are at 0.83 V and -0.74 V. The Dirac point can be deduced from the relations $E_{D_1} = 2E_{\mathrm{vHs}^+} - 2\hbar\Gamma K sin(\Theta/2)v_F + 2t - E_{D_2}$ and $E_{D_1} = 2E_{\mathrm{vHs}^-} + 2\hbar\Gamma K sin(\Theta/2)v_F - 2t - E_{D_2}$. We find a Dirac point at +0.18 eV in the first case and +0.12 eV in the second case. These values are quite close and more importantly they are positive. A close look at the spectroscopy in Fig. 3B shows a minimum in the dI/dV curve above the Fermi level around +0.18 V in good agreement with the calculated value from the vHs. Actually, we often observe a natural p-doping in some area of our pristine graphene samples (Fig. S8). This is in agreement with previous observations of natural p-doping of graphene grown on the carbon side of SiC [29, 30, 31, 32]. Further study is needed to fully understand the origin of this doping. The very low concentration of nitrogen atoms on the left region in Fig. 3A makes it plausible that the remaining doping level in this area is dominated by the initial p-doping of the pristine graphene sample. Therefore, this junction is a pn junction. Another example of a pn junction can be found in the supplementary materials (Fig. S9). Such junctions are observed more rarely than the nn' junctions described above. Further evidence of the nature of the junction is provided in Fig. 3C showing a mapping of point spectra taken across the pn junction. Firstly, the shift of the vHs at negative bias is clearly observable. The variation of the V_{vHs^-} position along the line extends over a distance of 5.5 nm as determined by the fitting curve (Fig. 3D) in good agreement with the junction width determined above. Secondly, the Dirac point can be seen in Fig. 3C as a dark trace at negative bias on the right side, shifting to positive bias on the left side. One can notice that across the junction, E_{vHs^-} varies from -0.79 eV to -0.66 eV (after renormalization by the phonon energy) corresponding to a variation of 0.13 eV. The Dirac point energy is varying from -0.14 eV to 0.12 eV (after renormalization by the phonon energy) corresponding to a total variation of 0.26 eV which is twice the energy variation of the vHs as expected from the relation above. We turn now to the link between the work function and the doping level. In Fig. 3E we show another sample area with a

nn' junction. The variation of the local work function can be followed by measuring the first field emission resonance (FER) peak obtained by dZ/dV spectroscopy measured in constant current mode. In Fig. 3F we show dZ/dV spectra revealing a peak at 4.15 V on the low doping part and at 4.09 V on the high doping part. This indicates that the work function decreases when the n doping increases. A visualization of the variation of the work function is obtained by measuring spectra at each point of the image of Fig. 3E and extracting the voltage value of the FER peak on each spectra. The resulting FER mapping is shown in Fig. 3E and clearly reveals a higher work function on the lower doping level area. This variation follows qualitatively the variation of the Dirac point as can be seen from the dI/dV spectra measured at the same location in Fig. 3G and from the Dirac point mapping shown in Fig. 3E. This variation is consistent with the expectation that increasing the n-doping level increases the Fermi energy and reduces the work function as sketched in Fig. 3H.

We have employed DFT to characterize the junction and its transport properties. We consider in Fig. 4A an ideal, sharply defined nn'-junction between two doped regions (0.06% N and 0.17% N) within the virtual crystal approximation[33]. The calculated potential shifts of the onsite p_z orbitals yield a spatial extent $4\Delta = 4.28$nm, constituting an ideal, lower bound to the experimental result above where additional broadening due to the tip convolution is expected, and in line with a pn junction model calculation based on the rigid band approximation[34]. This is suggesting that the width of the junctions determined in the experiment corresponds to the intrinsic width of such in-plane junctions, since it is close to the low limit obtained from the calculations. In Fig. 4B,C we consider the effect of a single N-atom placed near the "pristine" junction (Fig. 4A), resulting in a change in transmission and corrugation in the potential (dashed lines in Fig. 4C). We observe only minute changes in the transmission function for energies in the interesting energy region between the two Dirac points (zero points in Fig. 4B), while the scattering resonances due to the N are located $\sim$ 0.5eV away. We further show how the local bondcurrents are perturbed only in the vicinity of the N atoms (red lines in Fig. 4C).

3   Conclusion

In summary, we have shown that a C_{60} island monolayer can be used as a mask during plasma exposure of a graphene sample to achieve a nanostructuration of nitrogen dopants in graphene. We have shown that the nanostructuration results in the formation of unipolar (nn') and dipolar (pn) junctions in graphene. The typical width of the junctions interface is 7 nm and corresponds to sharp junctions with a width lower than the Fermi wavelength. We foresee that the submonolayer molecular resist technique presented here can be very versatile and is not limited to graphene. Hence, one can expect it to be effective on any other substrate where molecular self-assembly can be achieved such as transition metal dichalcogenides or other 2D van der Waals materials. Other chemical doping or functionalization with other species than nitrogen can also be envisaged. Moreover, this method can also be expanded to the effect of surface functionalization on other properties of materials that can be investigated with local probes such as forces or chemical activity.

4   Methods

Multilayer graphene samples were grown on a 6H-SiC wafer purchased from NovaSiC. The sample was first degassed under UHV conditions at 790° C during 5 hours. Further surface cleaning was achieved by annealing the sample at 850°C for 15 min under a silicon flux of $\sim$1 ML/min. The synthesis was then realized by annealing the sample at 1250° C during 5 min. After synthesis, the sample was transferred in air to the UHV system where low-temperature STM measurements were performed. The graphene sample was degassed under UHV at 850°C before further measurements and sample preparation.

The nitrogen-doping was performed by exposing the graphene sample to a flux of nitrogen radicals produced by a remote radio-frequency plasma source fed with N_2. The pressure in the chamber during doping was 5.10^{-4} mbar, the plasma power was 100 W. The plasma exposure time of the graphene sample was 10 minutes.

The deposition of C_{60} molecules was achieved by sublimation using an effusion cell (Dr. Eberl MBE-Komponenten GmbH) under UHV at 400° C onto the samples at the STM stage maintained at ~5 K. The graphene sample was then brought to room temperature allowing molecules to diffuse on the surface.

All STM measurements were performed with a low-temperature STM apparatus (Omicron) working at 4.6 K at a pressure lower than 1×10^{-10} mbar. The dI/dV spectra were acquired using a lock-in detector at a frequency of ca. 823 Hz and a modulation amplitude of 35 mV. The measurements were performed with an electrochemically etched tungsten tip. Before measuring on graphene, the tip was calibrated on a Au(111) surface until it showed the Shockley surface state feature in the spectroscopic measurements. Calculations of the Dirac point evolution (Fig. 2I) and charge isosurface along the model graphene unit cell have been performed using the very efficient Density Functional Theory (DFT) localized-orbital code Fireball [35]. This method uses a self-consistent version of the Harris–Foulkes LDA functional [36, 37], instead of the traditional Kohn–Sham functional based on the electronic density. In that respect, one approximates the total charge by a superposition of spherical charges around each atom. Also, Fireball uses a localized optimized minimal basis set [38], and the self-consistency is achieved over the occupation numbers through the Harris functional. The LDA exchange–correlation energy is calculated using the efficient multi-center weighted exchange–correlation density approximation (McWEDA) [39, 40]. Here, the cut-off radii for the wavefunctions' radial part (for s, sp and spd basis sets) defining the optimized basis set are the following (in atomic units): rs = rp = 4.5 and 4.2 for C and N atoms, respectively.

For the Dirac point evolution calculations, the graphene unit cell has been divided in thin nanoribbons of 74.4 Å length (width of the graphene unit cell) and about 6 Å width. The PDOS of each nanoribbon has been calculated and the minimum of the PDOS gives the values of the local Dirac point energy. Regarding the charge isosurface, we have calculated the full isosurface charge of the doped graphene unit cell to which we have substracted the full isosurface charge of the corresponding pristine graphene, without nitrogen atoms. The difference gives us the spatial repartition of the charge modification induced by the substituting nitrogen atoms.

The DFT and transport calculations in Fig. 4A were done using siesta/transiesta[41] with the GGA-PBE functional[42], periodic boundary conditions with 168 k-points (open boundary conditions) in the direction along (perpendicular to) the junction, and a SZP basis set.

Supporting Information
Supporting Information is available from the Wiley Online Library or from the author.

Acknowledgements

References

[1] L. S. Panchakarla, K. S. Subrahmanyam, S. K. Saha, A. Govindaraj, H. R. Krishnamurthy, U. V. Waghmare, C. N. R. Rao. Synthesis, Structure, and Properties of Boron- and Nitrogen-Doped Graphene. *Adv. Mater.* **21**, 4726 (2009).

[2] H. Wang, T. Maiyalagan, X. Wang. Review on recent progress in nitrogen-doped graphene: synthesis, characterization, and its potential applications. *Acs Catal.* **2**, 781 (2012).

[3] R. Yadav, C. K. Dixit. Synthesis, characterization and prospective applications of nitrogen-doped graphene: A short review. *J. Sci. Adv. Mater. Devices* **2**, 141 (2017).

[4] F. Joucken, L. Henrard, J. Lagoute. Electronic properties of chemically doped graphene. *Phys. Rev. Mater.* **3**, 110301 (2019).

[5] X. Zhou, A. Kerelsky, M. M. Elahi, D. Wang, K. M. Habib, R. N. Sajjad, P. Agnihotri, J. U. Lee, A. W. Ghosh, F. M. Ross, A. N. Pasupathy. Atomic-scale characterization of graphene p–n junctions for electron-optical applications. *ACS Nano* **13**, 2558 (2019).

[6] C. Gutiérrez, L. Brown, C.-J. Kim, J. Park, A. N. Pasupathy. Klein tunnelling and electron trapping in nanometre-scale graphene quantum dots. *Nat. Phys.* **12**, 1069 (2016).

[7] K.-K. Bai, J.-J. Zhou, Y.-C. Wei, J.-B. Qiao, Y.-W. Liu, H.-W. Liu, H. Jiang, L. He. Generating atomically sharp p-n junctions in graphene and testing quantum electron optics on the nanoscale. *Phys. Rev. B* **97**, 045413 (2018).

[8] D. J. Rizzo, S. Shabani, B. S. Jessen, J. Zhang, A. S. McLeod, C. Rubio-Verdú, F. L. Ruta, M. Cothrine, J. Yan, D. G. Mandrus, S. E. Nagler, A. Rubio, J. C. Hone, C. R. Dean, A. N. Pasupathy, D. N. Basov. Nanometer-Scale Lateral p–n Junctions in Graphene/-RuCl3 Heterostructures. *Nano Lett.* **22**, 1946 (2022).

[9] J. Lee, D. Wong, J. V. Jr, J. F. Rodriguez-Nieva, S. Kahn, H.-Z. Tsai, T. Taniguchi, K. Watanabe, A. Zettl, F. Wang, L. S. Levitov, M. F. Crommie. Imaging electrostatically confined dirac fermions in graphene quantum dots. *Nat. Phys.* **12**, 1032 (2016).

[10] J. Velasco, J. Lee, D. Wong, S. Kahn, H.-Z. Tsai, J. Costello, T. Umeda, T. Taniguchi, K. Watanabe, A. Zettl, F. Wang, M. F. Crommie. Visualization and control of single-electron charging in bilayer graphene quantum dots. *Nano Lett.* **18**, 5104 (2018).

[11] G. Li, H. T. Zhou, L. D. Pan, Y. Zhang, J. H. Mao, Q. Zou, H. M. Guo, Y. L. Wang, S. X. Du, H.-J. Gao. Self-assembly of C60 monolayer on epitaxially grown, nanostructured graphene on Ru (0001) surface. *Appl. Phys. Lett.* **100**, 4 (2012).

[12] M. Jung, D. Shin, S.-D. Sohn, S.-Y. Kwon, N. Park, H.-J. Shin. Atomically resolved orientational ordering of C 60 molecules on epitaxial graphene on Cu (111). *Nanoscale* **6**, 11835 (2014).

[13] J. C. Randel, F. C. Niestemski, A. R. Botello-Mendez, W. Mar, G. Ndabashimiye, S. Melinte, J. E. P. Dahl, R. M. K. Carlson, E. D. Butova, A. A. Fokin, P. R. Schreiner, J.-C. Charlier, H. C. Manoharan. Unconventional molecule-resolved current rectification in diamondoid–fullerene hybrids. *Nat. Commun.* **5**, 4877 (2014).

[14] E. J. Santos, D. Scullion, X. S. Chu, D. O. Li, N. P. Guisinger, Q. H. Wang. Rotational superstructure in van der Waals heterostructure of self-assembled C 60 monolayer on the WSe 2 surface. *Nanoscale* **9**, 13245 (2017).

[15] Z. Tan, D. Zhang, H.-R. Tian, Q. Wu, S. Hou, J. Pi, H. Sadeghi, Z. Tang, Y. Yang, J. Liu, Y.-Z. Tan, Z.-B. Chen, J. Shi, Z. Xiao, C. Lambert, S.-Y. Xie, W. Hong. Atomically defined angstrom-scale all-carbon junctions. *Nat. Commun.* **10**, 1748 (2019).

[16] G. Wang, M. Zhang, D. Chen, Q. Guo, X. Feng, T. Niu, X. Liu, A. Li, J. Lai, D. Sun, Z. Liao, Y. Wang, P. K. Chu, G. Ding, X. Xie, Z. Di, X. Wang. Seamless lateral graphene p–n junctions formed by selective in situ doping for high-performance photodetectors. *Nat. Commun.* **9**, 5168 (2018).

[17] M. Ishigami, J. H. Chen, W. G. Cullen, M. S. Fuhrer, E. D. Williams. Atomic Structure of Graphene on SiO2. *Nano Lett.* **7**, 1643 (2007).

[18] F. Joucken, Y. Tison, P. Le Fèvre, A. Tejeda, A. Taleb-Ibrahimi, E. Conrad, V. Repain, C. Chacon, A. Bellec, Y. Girard, S. Rousset, J. Ghijsen, R. Sporken, H. Amara, F. Ducastelle, J. Lagoute. Charge transfer and electronic doping in nitrogen-doped graphene. *Sci. Rep.* **5**, 14564 (2015).

[19] F. Joucken, Y. Tison, J. Lagoute, J. Dumont, D. Cabosart, B. Zheng, V. Repain, C. Chacon, Y. Girard, A. R. Botello-Méndez, S. Rousset, R. Sporken, J.-C. Charlier, L. Henrard. Localized state and charge transfer in nitrogen-doped graphene. *Phys. Rev. B* **85**, 161408 (2012).

[20] L. Zhao, R. He, K. T. Rim, T. Schiros, K. S. Kim, H. Zhou, C. Gutierrez, S. P. Chockalingam, C. J. Arguello, L. Palova, D. Nordlund, M. S. Hybertsen, D. R. Reichman, T. F. Heinz, P. Kim, A. Pinczuk, G. W. Flynn, A. N. Pasupathy. Visualizing individual nitrogen dopants in monolayer graphene. *Science* **333**, 999 (2011).

[21] V. D. Pham, F. Joucken, V. Repain, C. Chacon, A. Bellec, Y. Girard, S. Rousset, R. Sporken, M. C. d. Santos, J. Lagoute. Molecular adsorbates as probes of the local properties of doped graphene. *Sci. Rep.* **6**, 24796 (2016).

[22] Y. Zhang, V. W. Brar, F. Wang, C. Girit, Y. Yayon, M. Panlasigui, A. Zettl, M. F. Crommie. Giant phonon-induced conductance in scanning tunnelling spectroscopy of gate-tunable graphene. *Nat. Phys.* **4**, 627 (2008).

[23] Y. Zhang, V. W. Brar, C. Girit, A. Zettl, M. F. Crommie. Origin of spatial charge inhomogeneity in graphene. *Nat. Phys.* **5**, 722 (2009).

[24] S. Samaddar, I. Yudhistira, S. Adam, H. Courtois, C. B. Winkelmann. Charge Puddles in Graphene near the Dirac Point. *Phys. Rev. Lett.* **116**, 126804 (2016).

[25] J. Xue, J. Sanchez-Yamagishi, D. Bulmash, P. Jacquod, A. Deshpande, K. Watanabe, T. Taniguchi, P. Jarillo-Herrero, B. J. LeRoy. Scanning tunnelling microscopy and spectroscopy of ultra-flat graphene on hexagonal boron nitride. *Nat. Mater.* **10**, 282 (2011).

[26] S. C. Martin, S. Samaddar, B. Sacépé, A. Kimouche, J. Coraux, F. Fuchs, B. Grévin, H. Courtois, C. B. Winkelmann. Disorder and screening in decoupled graphene on a metallic substrate. *Phys. Rev. B* **91**, 041406 (2015).

[27] S. P. Milovanović, D. Moldovan, F. M. Peeters. Veselago lensing in graphene with a p-n junction: Classical versus quantum effects. *J. Appl. Phys.* **118**, 154308 (2015).

[28] I. Brihuega, P. Mallet, H. González-Herrero, G. Trambly de Laissardière, M. M. Ugeda, L. Magaud, J. M. Gómez-Rodríguez, F. Ynduráin, J.-Y. Veuillen. Unraveling the Intrinsic and Robust Nature of van Hove Singularities in Twisted Bilayer Graphene by Scanning Tunneling Microscopy and Theoretical Analysis. *Phys. Rev. Lett.* **109**, 196802 (2012).

[29] D. A. Siegel, C. G. Hwang, A. V. Fedorov, A. Lanzara. Quasifreestanding multilayer graphene films on the carbon face of SiC. *Phys. Rev. B* **81**, 241417 (2010).

[30] D. A. Siegel, C.-H. Park, C. Hwang, J. Deslippe, A. V. Fedorov, S. G. Louie, A. Lanzara. Many-body interactions in quasi-freestanding graphene. *Proc. Natl. Acad.* **108**, 11365 (2011).

[31] J. Hicks, M. Sprinkle, K. Shepperd, F. Wang, A. Tejeda, A. Taleb-Ibrahimi, F. Bertran, P. Le Fèvre, W. A. de Heer, C. Berger, E. H. Conrad. Symmetry breaking in commensurate graphene rotational stacking: Comparison of theory and experiment. *Phys. Rev. B* **83**, 205403 (2011).

[32] A. Tejeda, A. Taleb-Ibrahimi, W. d. Heer, C. Berger, E. H. Conrad. Electronic structure of epitaxial graphene grown on the C-face of SiC and its relation to the structure. *New J. Phys.* **14**, 125007 (2012).

[33] L. Bellaiche, D. Vanderbilt. Virtual crystal approximation revisited: Application to dielectric and piezoelectric properties of perovskites. *Phys. Rev. B* **61**, 7877 (2000).

[34] H. Yu, A. Kutana, B. I. Yakobson. Carrier delocalization in two-dimensional coplanar p–n junctions of graphene and metal dichalcogenides. *Nano lett.* **16**, 5032 (2016).

[35] J. P. Lewis, P. Jelínek, J. Ortega, A. A. Demkov, D. G. Trabada, B. Haycock, H. Wang, G. Adams, J. K. Tomfohr, E. Abad, H. Wang, D. A. Drabold. Advances and applications in the fireball ab initio tight-binding molecular-dynamics formalism. *Phys. Status Solidi B* **248**, 1989 (2011).

[36] J. Harris. Simplified method for calculating the energy of weakly interacting fragments. *Phys. Rev. B* **31**, 1770 (1985).

[37] W. M. C. Foulkes, R. Haydock. Tight-binding models and density-functional theory. *Phys. Rev. B* **39**, 12520 (1989).

[38] M. A. Basanta, Y. J. Dappe, P. Jelínek, J. Ortega. Optimized atomic-like orbitals for first-principles tight-binding molecular dynamics. *Comput. Mater. Sci.* **39**, 759 (2007).

[39] P. Jelínek, H. Wang, J. P. Lewis, O. F. Sankey, J. Ortega. Multicenter approach to the exchange-correlation interactions in ab initio tight-binding methods. *Phys. Rev. B* **71**, 235101 (2005).

[40] O. F. Sankey, D. J. Niklewski. Ab initio multicenter tight-binding model for molecular-dynamics simulations and other applications in covalent systems. *Phys. Rev. B* **40**, 3979 (1989).

[41] A. Garcia, *et al.*. Siesta: Recent developments and applications. *J. Chem. Phys.* **152**, 204108 (2020).

[42] J. P. Perdew, K. Burke, M. Ernzerhof. Generalized gradient approximation made simple. *Phys. Rev. Lett.* **77**, 3865 (1996).
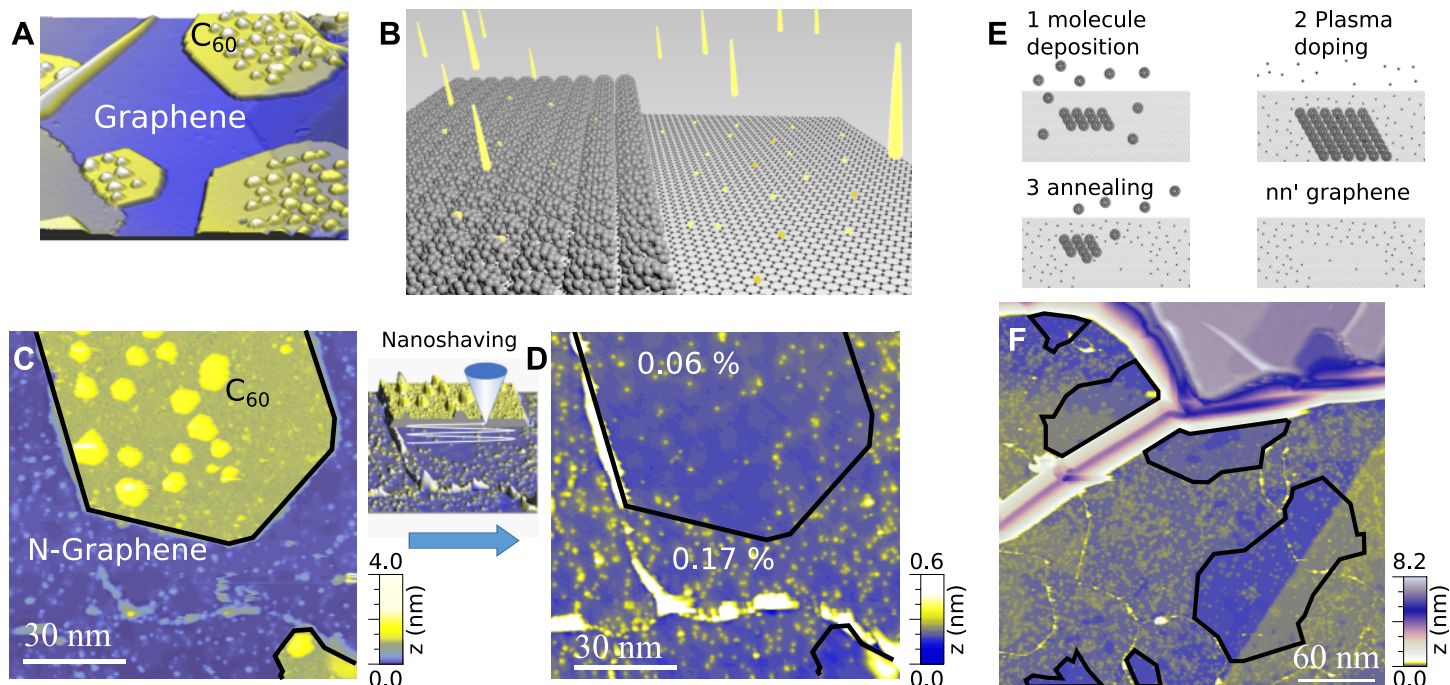
Figure 1: Submonolayer molecular resist for the nanostructuration of nitrogen dopants in graphene. **(A)** STM image of C_{60} islands on graphene on SiC(000$\bar{1}$) (2 V, 10 pA). **(B)** Schematic representation of the submonolayer resist technique consisting in using monolayer C_{60} islands as a mask during nitrogen plasma exposure of the sample. **(C)** STM image of graphene with a submonolayer of C_{60} after nitrogen plasma exposure (2 V, 10 pA). The area was then cleaned with the STM tip by nanoshaving (represented by the scheme on the right part). After this operation the distribution of nitrogen atoms on this area is revealed in the STM image shown in **(D)** (2 V, 50 pA). **(E)** Description of the process using sub-monolayer resist followed by thermal annealing to remove all the molecules, leaving the surface with nanodomains of low nitrogen concentration. **(F)** Large scale STM image of the sample after this treatement (2 V, 50 pA).
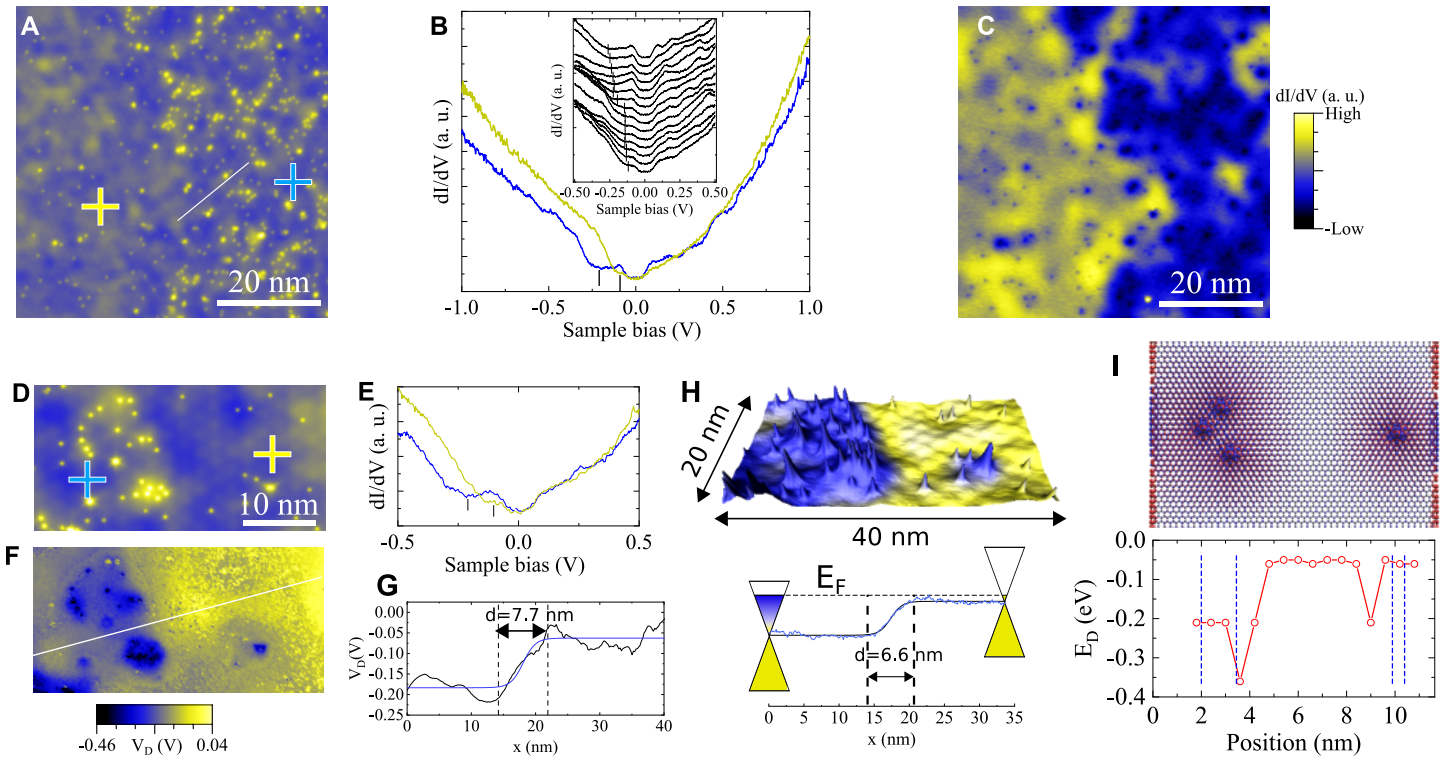
Figure 2: Unipolar junction in nitrogen-doped graphene. **(A)** Large scale STM image of a nn' graphene junction area (-0.3 V, 100 pA). **(B)** dI/dV spectra measured at positions marked by crosses in (A). The inset shows series of spectra measured along the white line in (A). **(C)** dI/dV map at -0.3 V measured simultaneously with the topography shown in (A). **(D)** Topographic STM image (-0.3V, 200 pA) of a junction taken at a different location than the previous one. **(E)** dI/dV spectra measured at positions marked by crosses in (D). **(F)** Mapping of the Dirac point extracted from spectra measured over the sample area shown in **(D)**. The white line indicate the line over which the profile shown in **(G)** has been measured, revealing the variation of the Dirac point position across the junction. **(H)** Top: 3D topographic STM image of the area (D) color coded with the conductance map at -0.3 V. Down: Sketch of the Dirac cones on both sides of the junction and linescan of the conductance map across the junction. **(I)** Atomic structure of the n-n' graphene junction used for charge redistribution, with 3 nitrogen atoms on one side and 1 nitrogen atom on the other side. The corresponding isosurface (10^{-4}eV/$Å^3$) is superimposed. The evolution of the calculated Dirac point energy along the n-n' junction is represented below.
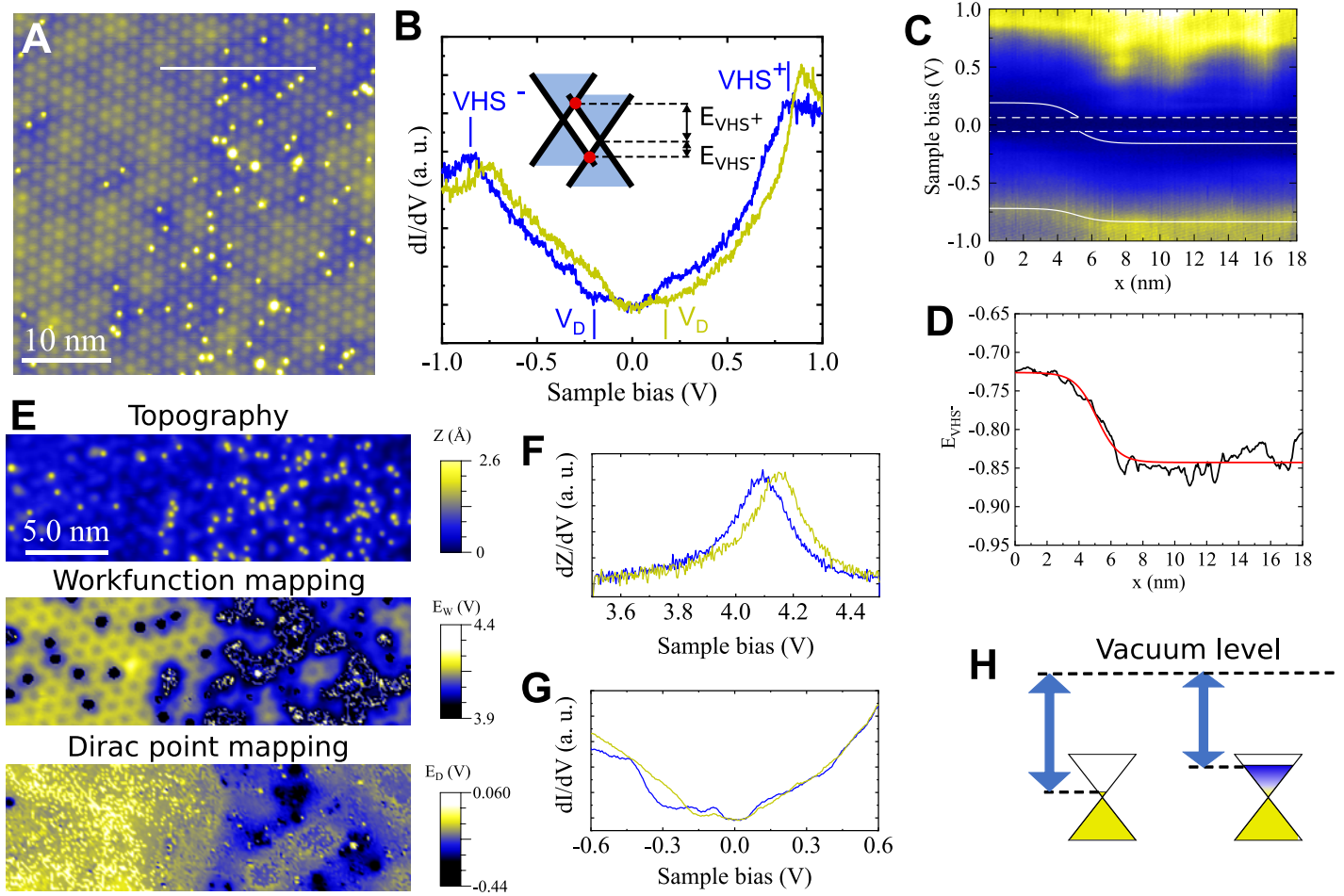
Figure 3: Van Hove singularities and work function through a graphene junction. **(A)** STM image (-1V, 500 pA) of a junction with low nitrogen concentration on the left, high concentration on the right. **(B)** dI/dV spectra on a high and low doped part of graphene. The inset represents the Dirac cones of the top (doped) and the underlying (undoped) layer. **(C)** dI/dV spectra mapping across the junction taken along the white line in panel (A). The white lines indicate the van Hove singularity and Dirac point positions. For the van Hove singularity we have used the fitting curve of panel (D), for the Dirac point we have applied the relation allowing to deduce E_D from E_{vHs^-} and we have plotted the corresponding voltage position of V_D. The dashed lines indicate the edges of the phonon gap-like feature. **(D)** Voltage position of the van Hove singularity at negative bias voltage along the dI/dV spectra mapping of panel (C) displayed together with a fitting curve (in red). **(E)** STM topograph of a graphene junction (0.5 V, 100 pA). Workfunction and Dirac point mapping on the same area obtained from the voltage of the first FER and the minimum in the dI/dV spectra, respectively. **(F)** dZ/dV spectra measured on a high doped (blue) and low doped (yellow) part of the graphene area shown in (E). **(G)** dI/dV spectra measured on a high (blue) and low (yellow) doped part of the area of panel (E). **(H)** Schematic representation of the workfunction variation with respect to the doping level of graphene.
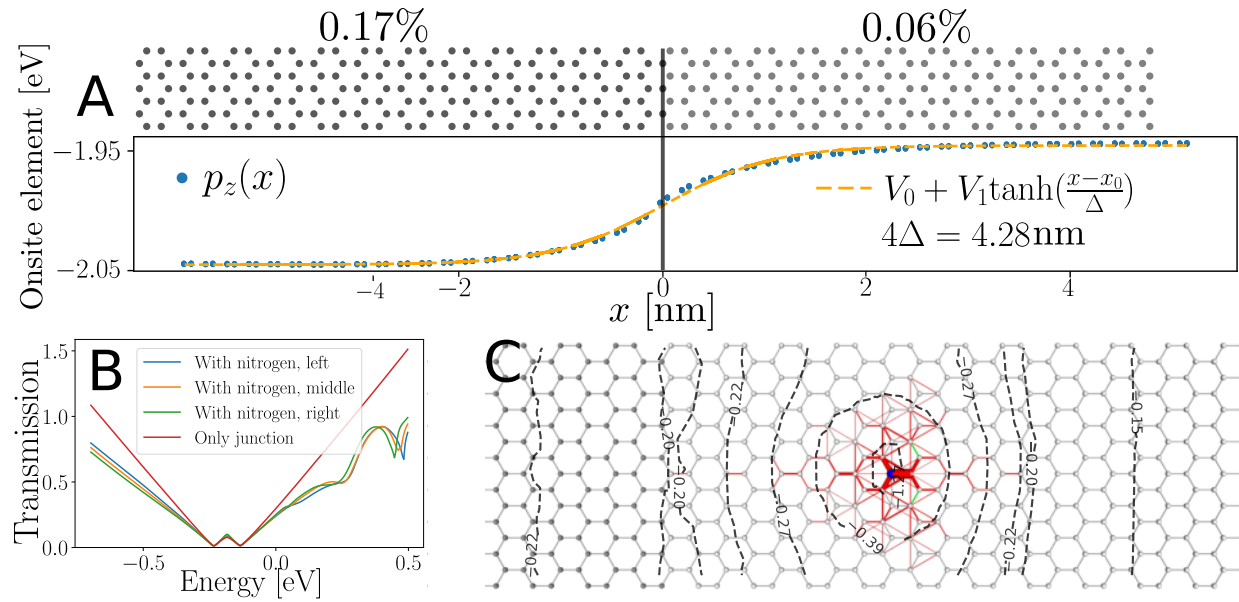
Figure 4: (A) DFT virtual crystal calculation of an ideal, abrupt nn' junction and p_z-onsite potential shifts yielding a junction width of 4.9 nm. (B) Transmission function of N placed in the n', middle, and n-parts of the abrupt junction, respectively. (C) N in the n-part. Change in electron bondcurrents ($E = -0.2$ eV) with N (red/green is a positive/negative changes). The contour lines show the spacial dependence and corrugation of the p_z onsite element.